Available online at www.sciencedirect.com
SCIENCE DIRECT®
ELSEVIER
Journal of Applied Geophysics 52 (2003) 75–91
JOURNAL OF APPLIED GEOPHYSICS
www.elsevier.com/locate/jappgeo

Near-field dipole radiation dynamics through FDTD modeling

Stanley J. Radzevicius[a,*,1], Chi-Chih Chen[b], Leon Peters Jr.[b], Jeffrey J. Daniels[c]

[a] *APA Division, ENSCO Inc., 5400 Port Royal Road, Springfield, VA 22151-2312, USA*
[b] *The Ohio State University ElectroScience Laboratory, 1320 Kinnear Road, Columbus, OH 43212, USA*
[c] *Mendenhall Laboratory, Department of Geological Sciences, The Ohio State University, 125 South Oval Mall, Columbus, OH 43210, USA*

Received 18 September 2001; accepted 30 October 2002

Abstract

We use finite-difference time-domain (FDTD) numerical simulations to study horizontal dipole radiation mechanisms and patterns near half-space interfaces. Time snapshots illustrating propagation of wavefronts at an instance in time are included with antenna patterns to provide a visualization tool for understanding antenna radiation properties. Near-field radiation patterns are compared with far-field asymptotic solutions and the effects of electrical properties, antenna height, and observation distance are investigated through numerical simulations. Numerical simulations show excellent agreement with measured data collected over a water-filled tank. Near-field H-plane radiation patterns are broader and contain radiation maxima beyond the critical angle predicted by far-field solutions. A large amplitude E-plane radiation lobe is located directly below the antenna in all simulations, while the two large amplitude sidelobes are less distinct and occur at larger incidence angles than predicted by far-field solutions. Radiation patterns resemble far-field solutions by a distance of 10 wavelengths, except near the critical angle where H-plane radiation maxima and E-plane sidelobes occur at larger incidence angles than predicted by far-field solutions.

Keywords: GPR; Radiation patterns; Dipole antennas; FDTD modeling

1. Introduction

Ground penetrating radar (GPR) is a non-destructive technique used to investigate a wide variety of subsurface environments. Dipoles are the most commonly used antennas because they are relatively straightforward to design and implement, are non-dispersive, and are linearly polarized. GPR antennas are not isotropic radiators or receivers and exhibit strong directionality of wavefields. High directivity adversely affects wide angle surveys used to determine velocity and other physical attributes. Coarse survey grids and highly directive radiation patterns can result in undetected targets located between survey lines. Directivity also influences tomography and migration results. Detailed antenna pattern information is of limited importance for simple anomaly detection surveys interested in determining the spatial

* Corresponding author.
E-mail address: radzevicius.stan@ensco.com (S.J. Radzevicius).
[1] Formerly Mendenhall Laboratory, Department of Geological Sciences, The Ohio State University, 125 South Oval Mall, Columbus, OH 43210, USA.

0926-9851/02/$ - see front matter © 2002 Elsevier Science B.V. All rights reserved.
doi:10.1016/S0926-9851(02)00241-0

distribution and burial depth of subsurface targets based on qualitative amplitude variations and time delays. Amplitude information becomes more important for imaging applications used to accurately determine the shape, orientation, and size of subsurface targets and becomes essential when inverting GPR data to extract physical property information.

The earliest GPR applications utilized radio echo sounders to map the thickness of glaciers in the Arctic and Antarctic as well as permafrost soil applications (Annan and Davis, 1976). Polar studies continue to be an important application of GPR (Arcone, 1996; Arcone and Delaney, 2000). Radar waves experience little attenuation in ice, and depth sounding of several kilometers are possible on polar ice sheets. Far-field radiation patterns can readily be utilized in these ideal environments. The shallow subsurface is increasing in importance for engineering, environmental, archaeological, landmine, and unexploded ordinance investigations. The depths that are of interest for these investigations are commonly measured in centimeters or meters and far-field solutions do not accurately describe radiation patterns in the near-surface. Shallow targets and attenuation of radar waves by lossy soils, especially clay-rich soils, limit investigation depths for these applications (Hoekstra and Delaney, 1974; Olhoeft, 1987, 1998; Davis and Annan, 1989).

Historically, GPR data had been processed and imaged using standard acoustic algorithms from seismic reflection processing that assume that the source and receiver emit and receive fields equally in all directions. While source and receiver directivity does not obviate imaging algorithms based on isotropic radiators, improved results may be obtained by taking into account radiation patterns. Several publications have investigated the incorporation of far-field interfacial dipole radiation patterns into acoustic Kirchhoff migration algorithms to improve GPR imaging (Moran et al., 2000; van Gestel and Stoffa, 2000). van der Kruk (2001) utilized the vectoral nature of GPR fields and incorporated antenna radiation patterns. Lehmann et al. (2000) suggested that the directional nature of GPR radiation patterns could be reduced by combining vector fields from two orthogonal antenna pattern planes to create a ''pseudo scalar'' wavefield. This was accomplished with parallel transmitter–receiver antennas by combining orthogonal coincident data sets.

While target detection and depth determination may be sufficient for some GPR applications, quantitative amplitude and polarization information from scattered fields observed at multiple incidence and scattering angles can be used to constrain the size, shape, and electrical properties of buried objects. Accurate antenna pattern information is needed to correct for antenna directivity in these applications. Amplitude variation with offset (AVO) analysis of GPR data has been proposed to constrain physical properties. Amplitude variation with offset (AVO) analysis of seismic data is commonly used to constrain physical properties for hydrocarbon exploration. Several papers have suggested a similar approach for GPR applications by utilizing Fresnel reflection coefficients in place of Zoeppritz equations (Baker, 1998; Reppert et al., 2000). The limited understanding of near-surface GPR radiation patterns has hindered application of AVO concepts.

Understanding the radiation patterns of dipole antennas near a planar boundary between two semi-infinite media has long been an important subject for ground penetrating radar research and applications. Sommerfeld (1909) first published asymptotic far-field solutions for an infinitesimal dipole as early as 1909. The inability to solve the Sommerfeld integral using closed form analytical solutions has resulted in many different approximations and numerical solutions. Far-field approximations to the Sommerfeld integral have been an active area of research for many years (Norton, 1936, 1937a,b; Baños, 1966; Wait, 1962; Annan, 1973; Annan et al., 1975; King et al., 1974; Bannister, 1982; Engheta et al., 1982; Smith, 1984; Wensink et al., 1990; Arcone, 1995; Baumann and Sampaio, 2000; Jiao et al., 2000).

The advent of faster computers in the 1990s and increasing near-surface GPR applications resulted in numerical approximations of the Sommerfeld integral that include near-field terms (van der Kruk and Slob, 2000; van der Kruk, 2001; Valle et al., 2001). The improved computational resources of the 1990s also made finite-difference time-domain (FDTD) modeling of antenna patterns feasible (Luebbers and Beggs, 1992; Maloney and Smith, 1992; Roberts, 1994; Turner, 1994; Nehrbass, 1996; Roberts and Daniels, 1996; Lampe and Holliger, 2000, 2001; Radzevicius, 2001). Although FDTD simulations are more computationally intensive than some other

numerical solutions, they provide additional insight into antenna radiation mechanisms by visualizing the propagation of electric and magnetic fields as a function of time and space as the computations proceed.

The literature is filled with discrepancies of when far-field asymptotic solutions accurately describe antenna patterns and range from a few wavelengths to greater than 40 wavelengths. It is important to test the ability of analytical and numerical solutions to accurately describe radiation patterns through physical measurements. Published studies based on physical measurements in a water tank by Wensink et al. (1990) indicate that far-field conditions only start to develop at a radius of at least 30 wavelengths. Smith (1984) measured broader radiation patterns than predicted from far-field solutions at a distance of 8.1 wavelengths in water. The discrepancy between measured and far-field theoretical results was attributed to measured patterns not being far-zone patterns. Simulations by Valle et al. (2001) show incomplete convergence to far-field solutions at 40 wavelengths. The limited understanding of near-field antenna patterns and lack of publications on the subject prompted us to investigate near-field radiation patterns through numerical modeling and physical measurements.

2. Finite-difference time-domain modeling of antenna radiation mechanisms

We used a differentiated Gaussian pulse (Fig. 1) as the input signal to feed an infinitesimally small horizontal dipole for the FDTD simulations. The grid was composed of Yee cells (Yee, 1966), the FDTD equations were second order in space and time, and the model was run at 98% of the Courant stability criterion (Kunz and Luebbers, 1993).

The fields radiated by an infinitesimally small horizontal dipole located on an air–soil interface characterized by a relative permittivity ($\varepsilon_r = 5$) and conductivity ($\sigma = 0$ S/m) are illustrated in Fig. 2 with a snapshot in time through the H-plane. A relative permittivity of 5 was used for the simulation because it is characteristic of a sandy soil. The H- and E-planes are vertical planes orthogonal and parallel to the long axis of the horizontal dipole, respectively. Spherical body waves are observed propagating radially upward into the air and downward into the subsurface. Because the velocities of the two media are different, boundary waves are created to maintain continuity of electric and magnetic flux densities normal to the interface, as well as continuity of tangential electric and magnetic fields across the interface. A head wave (lateral wave) is formed in the subsurface with a

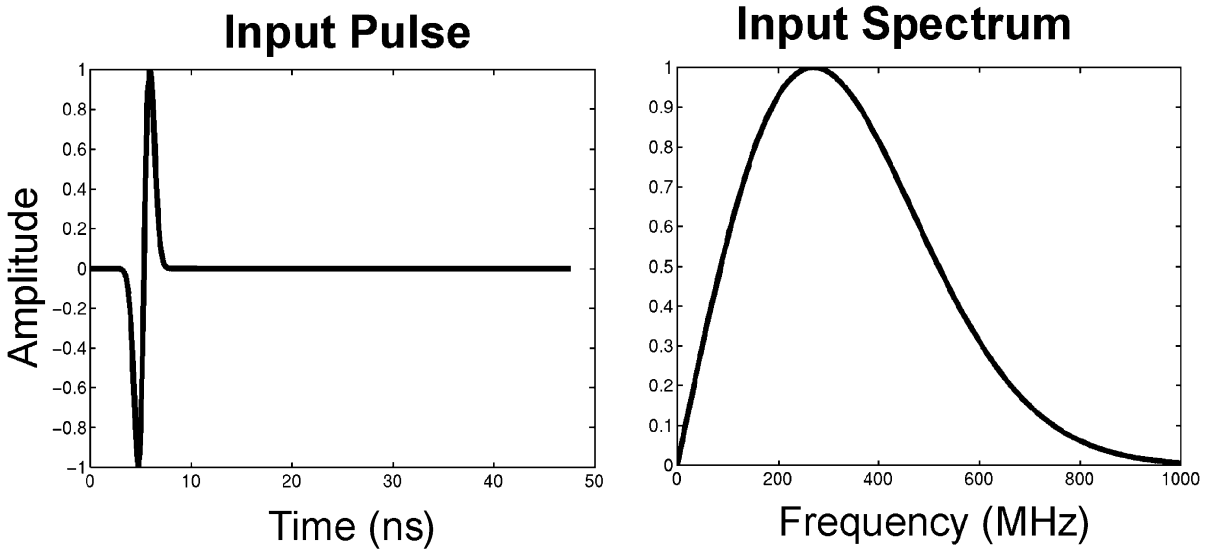

Fig. 1. Differentiated Gaussian input pulse and spectrum used in FDTD simulations.

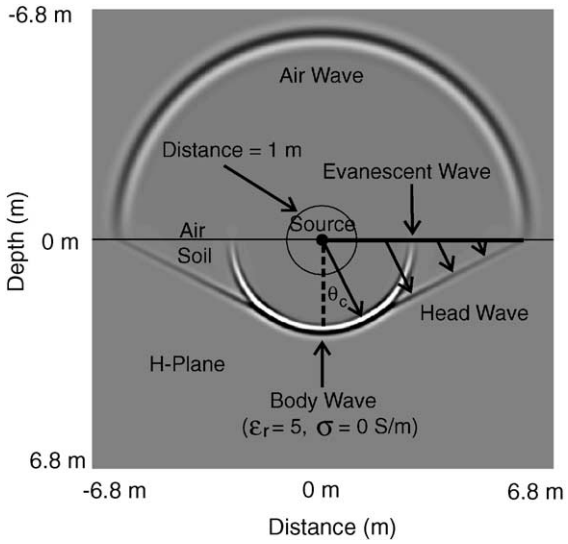

Fig. 2. H-plane snapshot of FDTD-calculated fields for a source located directly on an air–soil (soil $\varepsilon_r = 5$, $\sigma = 0$ S/m) interface.

direction of propagation at the critical angle of the air–ground boundary ($\theta_c \sim 26.5°$) and is coupled to the spherical air wave. The head wave spreads as a truncated cone in 3D and arises from energy refracting into the subsurface at the critical angle. These conical wavefronts start at the tangent circle on the body wave wavefront and end at the interface. The tangent circle where the body waves and head waves intersect each other occurs at the critical angle position. An evanescent wave that is coupled to the spherical body wave in the ground travels in the air with a velocity of a wave propagating horizontally in the ground. The evanescent wave is not clearly visible at the scale of this snapshot because it decays exponentially away from the interface and is only easily observed in close proximity to the interface. The evanescent wave is more readily observed in the FDTD wide angle reflection and refraction (WARR) radargram simulated by keeping the transmitting antenna stationary and recording fields directly above the air–ground interface (Fig. 3). The evanescent wave, commonly referred to as a direct ground wave on radargrams, appears as a linear event with the velocity of a wave propagating horizontally in the ground. Another linear event propagating at the speed of light in air is produced by the spherical air wave. A hyperbola produced by spherical body waves reflecting from a 3.75 m^2 perfectly conducting plane buried at a depth of 1.07 m is also observed.

Radiation patterns for this paper are obtained from fields computed along a sphere of constant radius

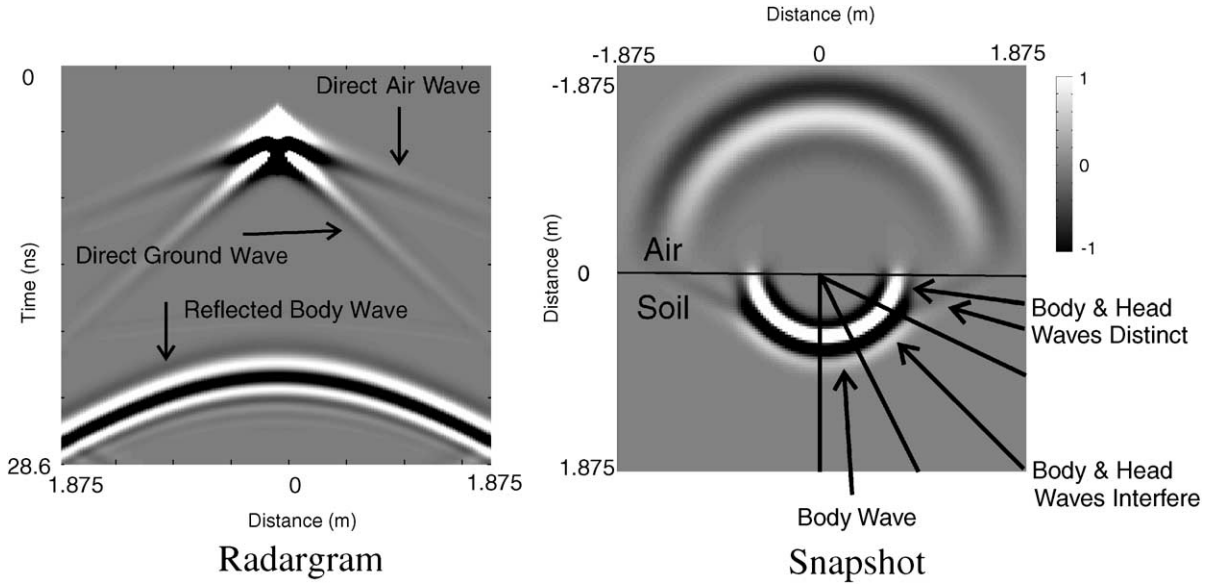

Fig. 3. Wide angle reflection and refraction radargram simulation (left) and snapshot (right).

using a 3D FDTD cube. Because radiation patterns are a function of observation distance, fields are recorded in the time-domain along a sphere of constant radius and Fourier transformed into the frequency-domain to study antenna patterns at different observation distances in terms of wavelength. From the FDTD simulations (Figs. 2 and 3), it is apparent that body waves and head waves interfere to produce the composite antenna patterns in the subsurface. For a given frequency, the radiation pattern is determined by the interference between the body and head wave mechanisms. For instance, near the downward direction (normal to interface), the pattern is determined by the body waves alone (Fig. 3). As the angle increases and

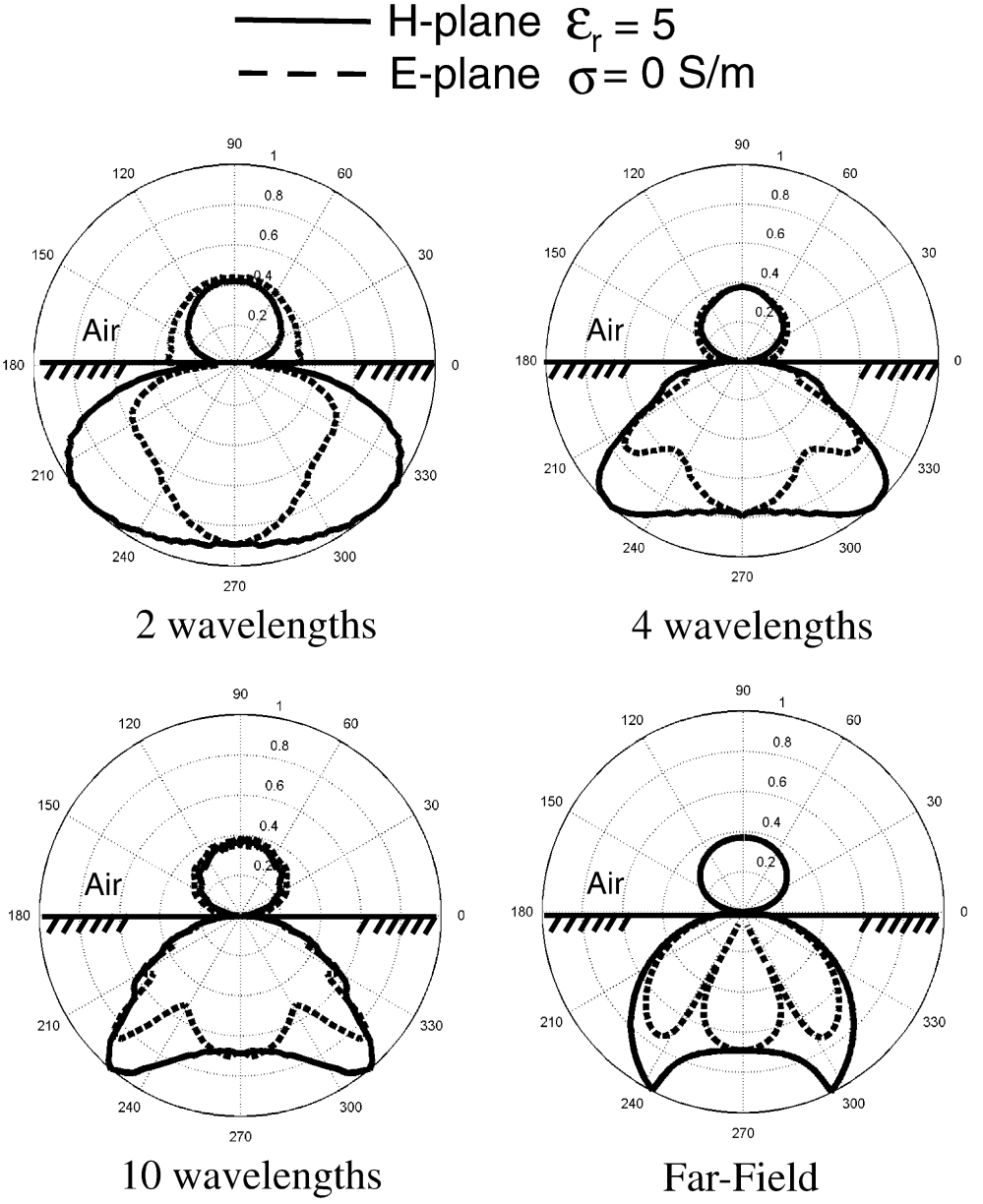

Fig. 4. H- and E-plane radiation patterns as a function of observation distance in terms of wavelength for a sandy soil.

moves away from the normal direction, the pattern is determined by the relative magnitude and phase (or time separation) differences between the body and head wave mechanisms. Frequency-domain patterns are composed of monofrequency amplitude values, and as a result, body and head wave contributions cannot be separated. In the time-domain, the body and head waves appear as distinct events separated in space and time, except for a region of interference that exists beyond the critical angle where body and head waves cannot be separated in space and time (see Fig. 3). Because radiated GPR pulses have a finite duration, a region of interference exists beyond the critical angle where body and head waves cannot be easily separated in space and time (Fig. 3). Body and head waves become easier to separate in space and time with increasing observation distance, increasing soil permittivities, and increasing incidence angles.

Polar H- and E-plane antenna pattern plots for an infinitesimal horizontal dipole located on a half-space with a soil characterized by a relative dielectric permittivity ($\varepsilon_r = 5$) and a conductivity ($\sigma = 0$ S/m) are shown in Fig. 4 as a function of observation distance in terms of wavelength. Asymptotic far-field solutions derived from analytical solutions are also plotted. The sharp peaks and notches characteristic of asymptotic far-field solutions are not observed in FDTD simulations. Far-field solutions predict sharp lobes at the critical angle for the H-plane. E-plane far-field solutions contain a large lobe directly below the antenna along with amplitude lows at the critical angle and two large sidelobes located beyond the critical angle. Compared to far-field patterns, near-field H-plane patterns are broader and contain amplitude highs beyond the critical angle. Directivity increases and radiation lobes slowly approach the critical angle position with increasing observation distance. A large E-plane radiation lobe is located directly below the dipole in all simulations. The two large sidelobes become more distinct and move downward toward the far-field position with increasing observation distance. Numerous small amplitude sidelobes develop

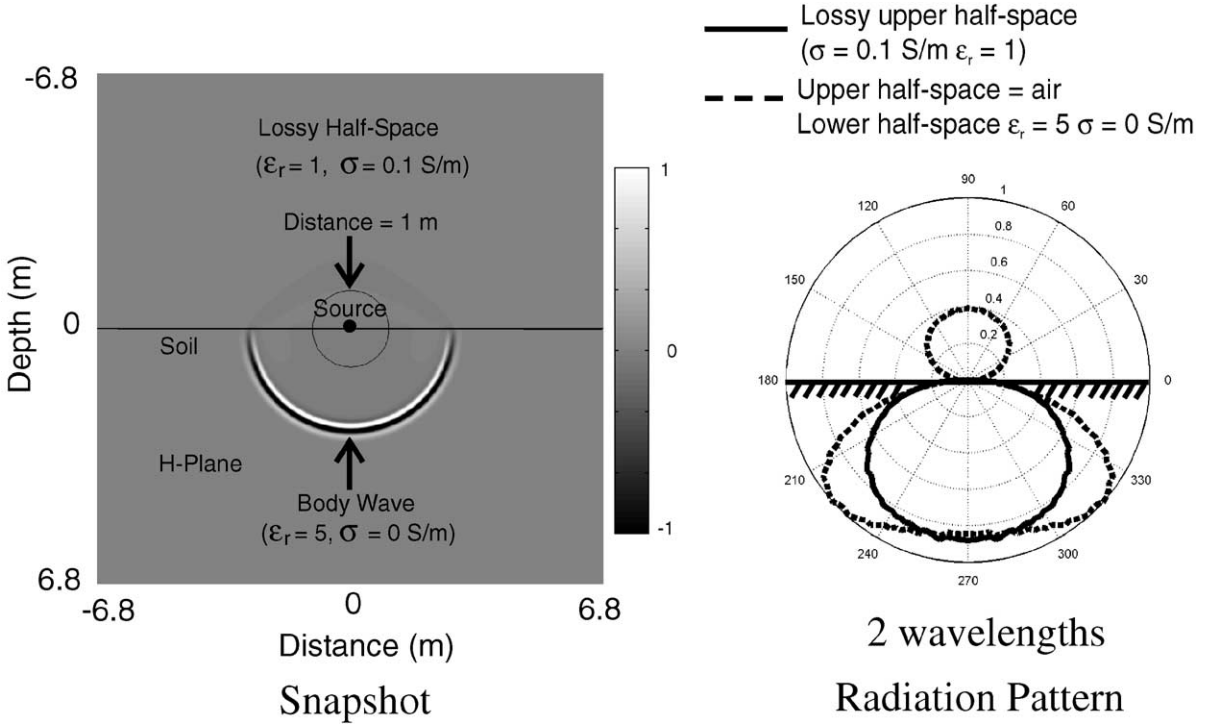

Fig. 5. Snapshot and radiation pattern showing simplified radiation pattern produced by a lossy upper half-space.

beyond the critical angle position in both the H- and E-plane patterns with increasing observation distance. The sidelobes result from the interference between body and head waves. Increasing observation distance increases phase (time separation) differences between body and head waves and increases the number of sidelobes.

The head wave can be reduced or removed from the FDTD simulations by making the upper half-space lossy. Because head waves are produced by energy traveling in the upper half-space and refracting into the lower half-space at the critical angle, loss in the upper half-space reduces energy radiated into the lower medium. An upper half-space characterized by a relative dielectric permittivity and a conductivity ($\varepsilon_r = 1$, $\sigma = 0.1$ S/m) greatly reduces the air wave in the upper half-space and nearly eliminates the head wave from the lower half-space (Fig. 5). A lossy upper half-space reduces antenna pattern lobes and results in a simplified pattern (Fig. 5). The simplified radiation pattern may result from the combination of removing the head wave and modifying the body waves by adding a conductive material above the dipole. Incorporating a lossy material above the radiating dipole may be used to design antennas with more desirable radiation patterns. Maintaining a low dielectric permittivity, in addition to a high conductivity above the ground, will simplify radiation patterns and maximize the amount of energy radiated into the subsurface.

Because GPR antennas are not always located directly on the half-space interface, the effects of placing the source above and below the interface are investigated. These studies also provide further insight into radiation pattern mechanisms. Raising the source 0.165 m in air above the interface results in direct and reflected air waves that will interfere with each other

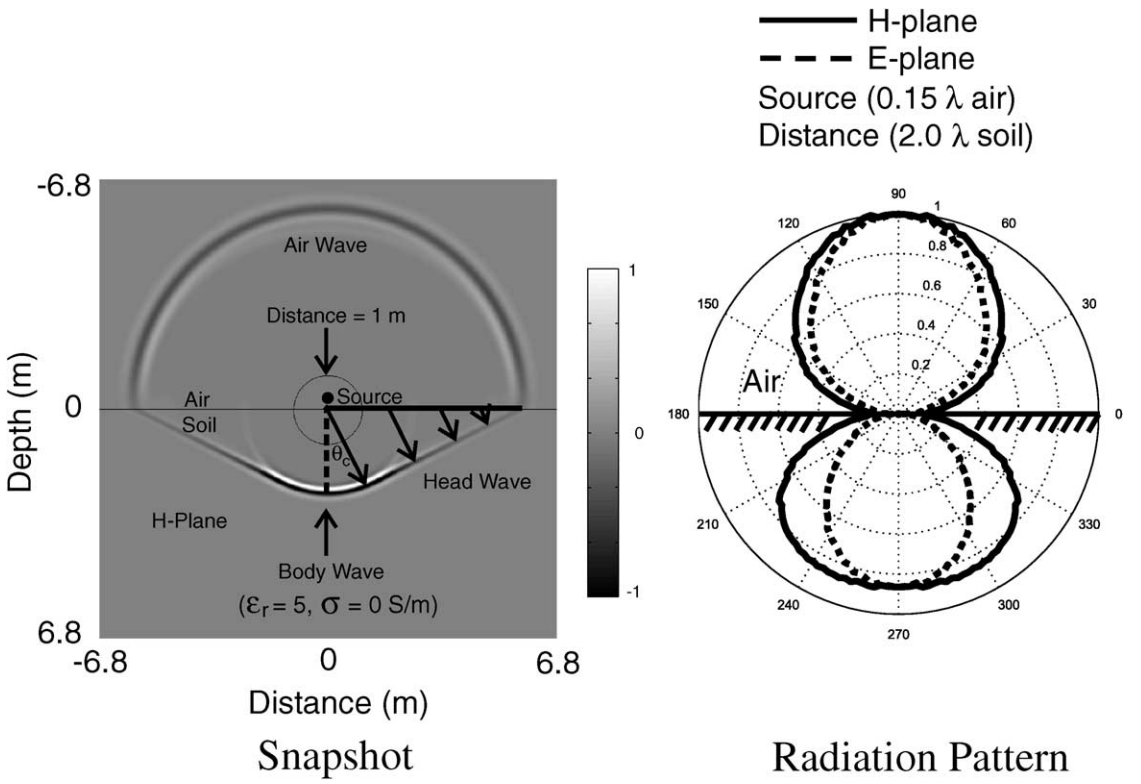

Fig. 6. Snapshot and radiation patterns for a source raised above the interface showing increased directivity produced by attenuation of energy refracted beyond the critical angle.

constructively or destructively, depending on the source height in terms of wavelength. Because refracted body wave energy beyond the critical angle in the ground is evanescent, body wave energy beyond the critical angle is highly attenuated (Fig. 6). The reduction in body wave energy beyond the critical angle is the primary factor for increased antenna pattern directivity (Fig. 6). In addition to increased antenna pattern directivity, lifting an antenna above the interface increases the percentage of energy radiated into the air relative to the subsurface (Figs. 4 and 6).

The effect of placing a source in the high permittivity, lower half-space is illustrated in Fig. 7. The air wave now consists of a refracted wave, and the subsurface body waves consist of a directly radiated wave and a wave reflected from the interface. Head waves are now excited by body waves reflected from the interface at angles equal to or greater than the critical angle. The lobes in the antenna patterns are now primarily produced by the interference of direct and reflected body waves (Fig. 7). The number of sidelobes increases with observation distance in terms of wavelength.

The above FDTD snapshots and antenna pattern plots provide a better understanding of the physical mechanisms that produce antenna patterns as a function of antenna position relative to a half-space interface and observation distance in terms of wavelength. Because it is important to test the ability of numerical results to simulate physical measurements, we first describe the measurements we used to test the FDTD results before discussing the effects of varying electrical properties on antenna patterns.

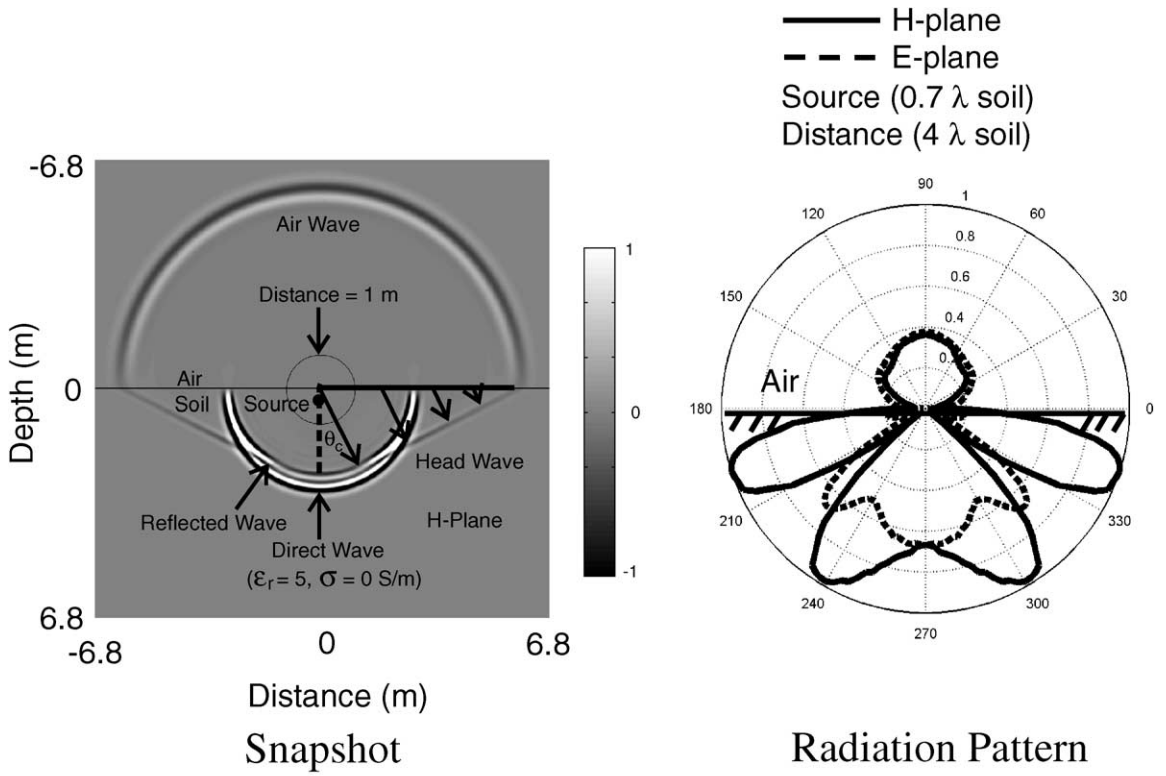

Fig. 7. Snapshot and radiation patterns showing radiation lobes resulting from the interference of direct and reflected body waves when the source is located in the higher permittivity medium.

3. Physical measurements and comparison with modeled results

We conducted experiments to validate the FDTD models. Measurements were conducted over a fluid because it is more homogeneous and it allowed for easy movement of probing targets and antennas in the lower half-space. The probing target was moved at a constant radius, eliminating the need for attenuation and spreading corrections. A 0.17-m long, 10° bow-tie antenna (Fig. 8) located on an air–water interface was used as the antenna under test (AUT), as shown in Figs. 9 and 10. The antenna flare angle was adjusted to provide an impedance match over the water and a hybrid balun was used to balance the antenna. A cylindrical polyethylene tank having a height of 1.2 m and a diameter of 2.4 m was filled with water characterized by a relative dielectric permittivity ($\varepsilon_r = 80$) and conductivity ($\sigma =$ 0.027 S/m) at 60 MHz.

A rotating arm constructed of PVC pipe drilled with holes to allow water to enter the portion of the structure that was submerged, and thus lower the fields scattered from the PVC pipe, served as the supporting structure for the probing target. The radiation pattern was determined by measuring the backscattering from the probing target. In contrast to the direct-probing technique that uses a field-probing antenna, no cable is present to cause measurement error. The probing target consisted of a narrow rectangular metallic plate (0.04×0.75 m) facing toward the AUT. The probing target orientation with respect to the AUT was held constant to maintain a consistent scattering pattern from the target probe.

Fig. 9. Photograph of antenna test facility.

A swept frequency network analyzer was used to transmit and receive the electromagnetic signals via the AUT. The data were collected in the frequency-domain using a sweep consisting of 1-MHz increments between 35 and 435 MHz. A personal computer was used to record data and control the motor and network analyzer that recorded data at 1° increments up to 5° below the air–water interface. The network analyzer and feed cable were calibrated by adding a short, open, and matched load to the end of the feed cable. A background measurement with no target present was used to remove scattering from the tank walls. The data were Fourier transformed into the time-domain and

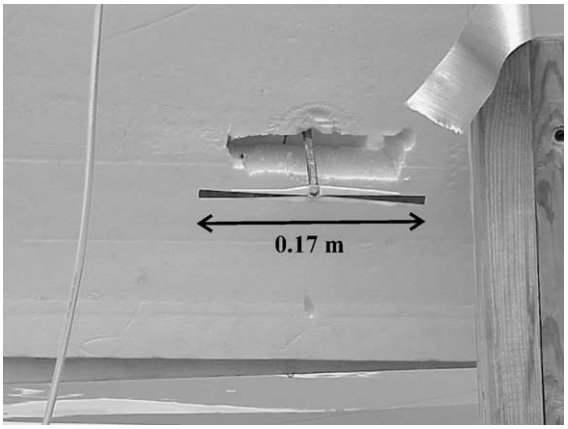

Fig. 8. Photograph of antenna under test.

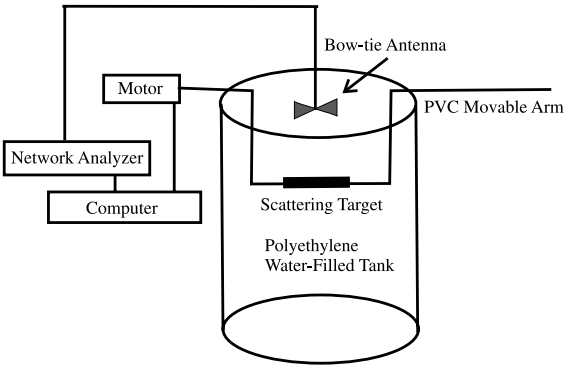

Fig. 10. Scheme of experimental setup for measuring antenna patterns over a water-filled tank.

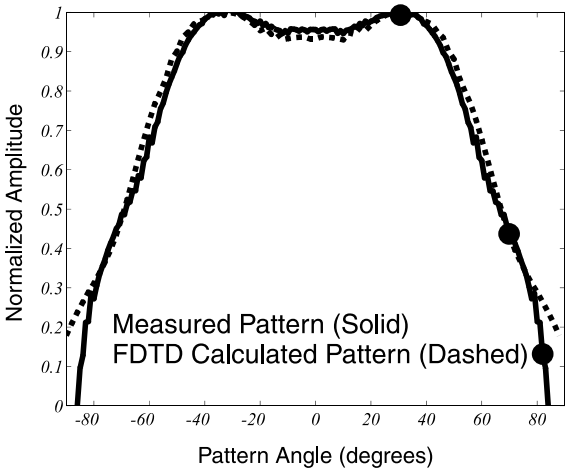

Fig. 11. Comparison of measured (solid) and directly computed FDTD (dashed) H-plane antenna patterns at a radial distance of two wavelengths in water at 100 MHz ($\varepsilon_r = 80$, $\sigma = 0.027$ S/m). A metallic pipe was introduced into the FDTD model to simulate probe–interface interactions (dots).

range gate was used to isolate any remaining interactions between the probing target and the tank. The calibrated data were then Fourier transformed back into the frequency-domain so that antenna patterns could be determined for each frequency.

A comparison of normalized measured (solid) and 3D FDTD infinitesimal electric dipole (dashed) antenna patterns at a distance of 2 wavelengths in water ($\varepsilon_r = 80$, $\sigma = 0.027$ S/m) at 100 MHz are shown in Fig. 11. The 0° is located directly below the antenna and ±90° represents the air–water interface. The measured and directly calculated FDTD data show excellent agreement for angles up to 80° (10° from the interface). While small field values for angles above 80° produce some measurement error, probe–interface interaction for angles above 80° (Fig. 12) results in discrepancies between calculations based on direct measurements and those based on backscattering. A metallic pipe was introduced into the FDTD model (Fig. 12) to simulate the physical experimental back-

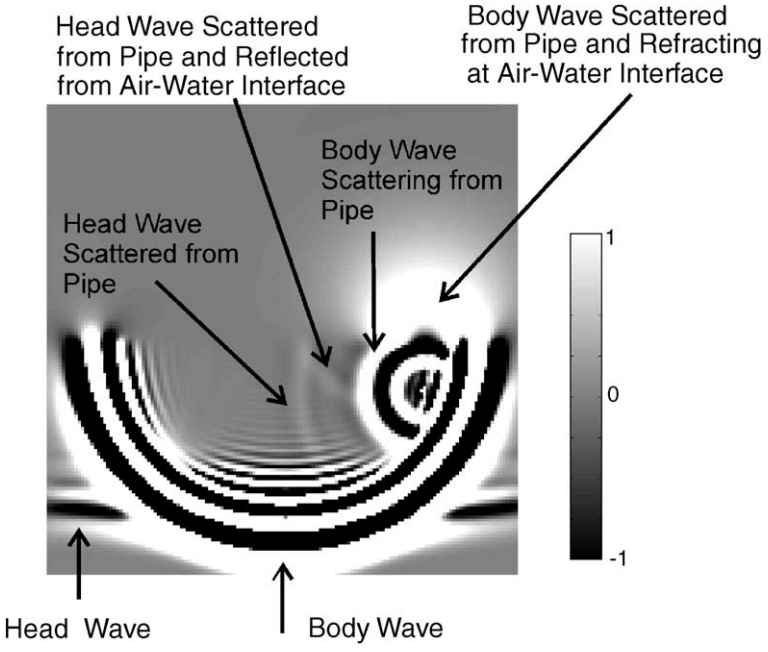

Fig. 12. Snapshot from FDTD simulation illustrating the effect of the air–water interface on antenna pattern backscattering measurements near the interface. Backscattering measurements underestimate radiation patterns near the interface because of energy scattering and refracting across the interface.

scattering measurements, and the results are shown on Fig. 11 as three dots. Patterns based on direct and backscattering calculations show excellent agreement for angles up to 80°. For angles beyond 80°, the probe–interface interactions result in reduced backscattered amplitudes. The effects of electrical properties on antenna patterns can now be studied using the validated FDTD tool.

4. Effects of electrical properties on antenna patterns

Radiation patterns for a horizontal dipole located on a high permittivity half-space ($\varepsilon_r = 80$, $\sigma = 0$ S/m) as a function of observation distance are shown in Fig. 13 along with the asymptotic far-field solutions. Increased directivities occur in water characterized

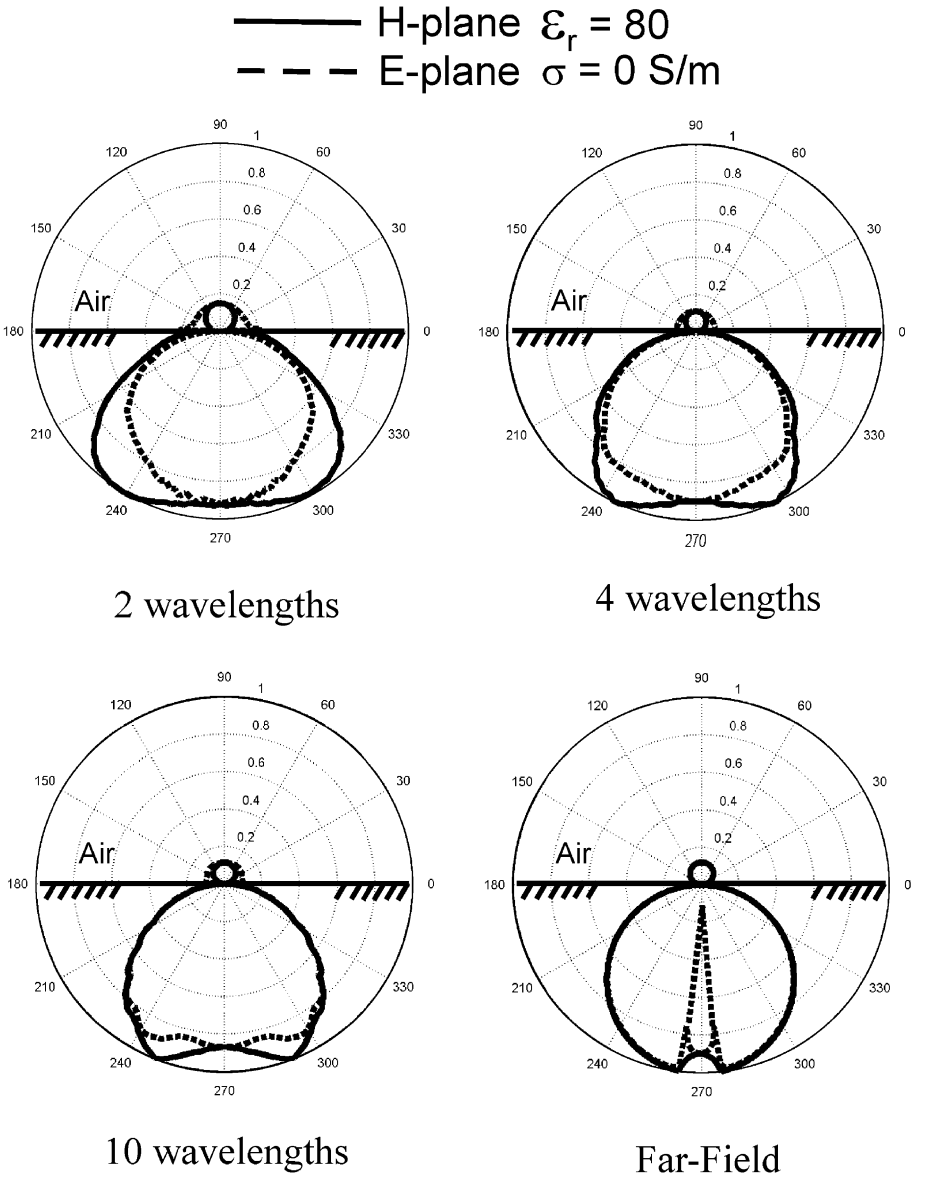

Fig. 13. H- and E-plane radiation patterns as a function of observation distance in terms of wavelength for water.

by a large permittivity ($\varepsilon_r = 80$, Fig. 13) compared to a sandy soil with a small permittivity ($\varepsilon_r = 5$, Fig. 4). Peak H-plane amplitudes occur beyond the critical angle and slowly approach the asymptotic far-field solutions for each of the permittivities. The two large amplitude E-plane sidelobes become less distinct as permittivity increases. FDTD simulations show good agreement with patterns measured by Smith (1984) at a distance of 8.1 wavelengths in water (Fig. 14).

While electrical conductivity is nonzero for all soils, it does not obviate radiation pattern results obtained from simulations based on zero electrical conductivity. Near-field simulations suggest that the primary influence of conductivity on radiation pattern amplitudes is the amplitude decay from conduction losses which result in a larger percentage of energy radiated into the air relative to the subsurface (Fig. 15). Our near-field measurements over lossy water

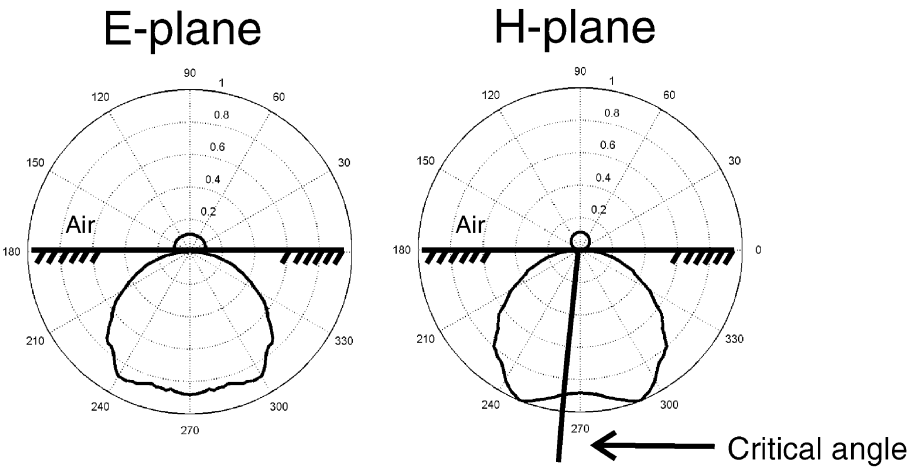

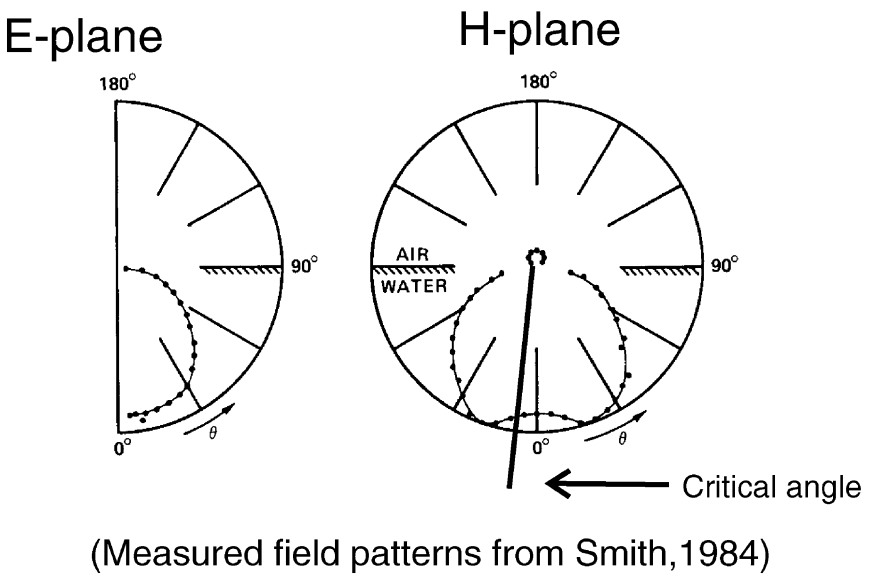

Fig. 14. FDTD simulations show good agreement with published measured results of Smith (1984).

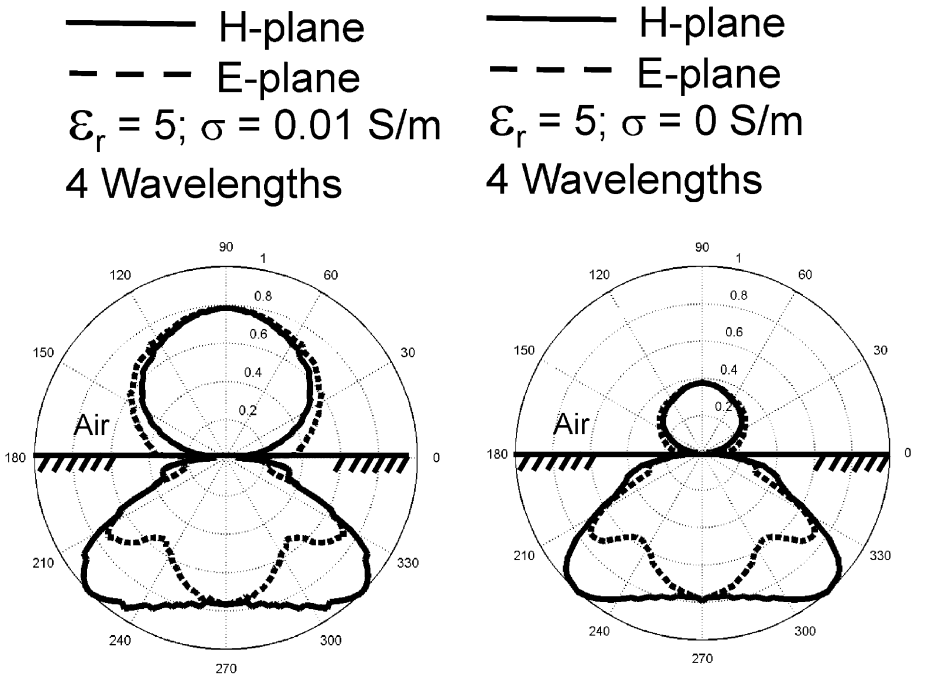

Fig. 15. Comparison of radiation patterns with zero and nonzero electrical conductivity.

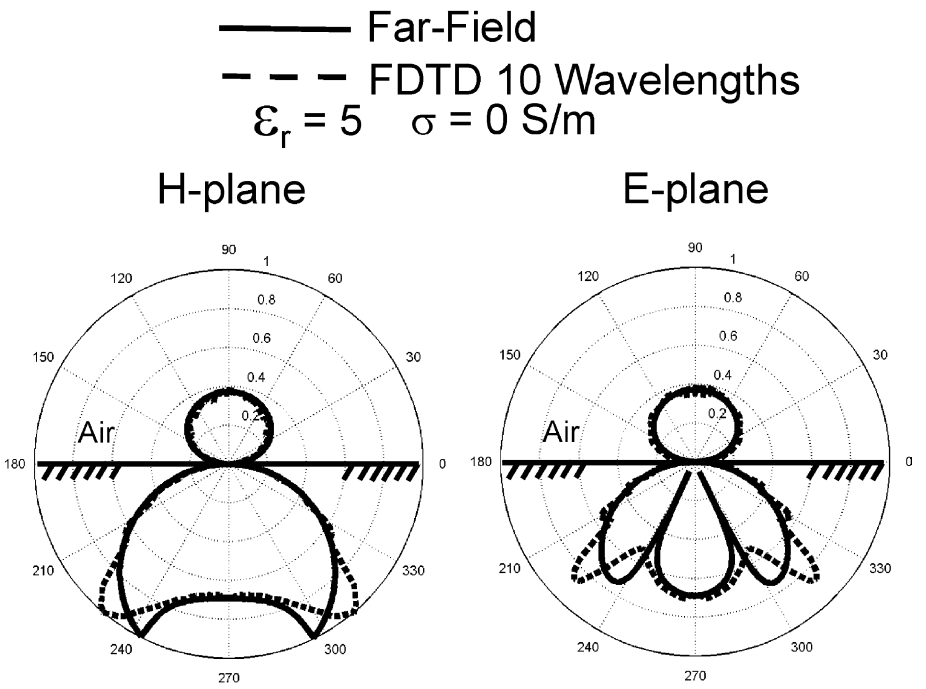

Fig. 16. Superposition of far-field and FDTD radiation patterns computed for a distance of 10 wavelengths illustrating the convergence toward far-field solutions.

($\sigma = 0.027$ S/m) confirm these results by showing measured antenna pattern shapes similar to those obtained from zero conductivity models. Minor sidelobe development (amplitude relative to main lobes) becomes more prominent at large observation distances and results from the increased importance of head waves with increasing conductivity and distance traveled. Body waves attenuate more rapidly than head waves because the total travel path of body waves is confined to the lossy medium.

While conductivity did not significantly affect the position of major radiation lobes in the near-surface simulations performed, dielectric permittivity affected the position of major radiation lobes in all simulations. Radiation patterns resemble far-field solutions for distances beyond 10 wavelengths, except near the critical angle position where H-plane peaks and E-plane sidelobes occur at larger incidence angles than predicted by far-field solutions (Figs. 4 and 13). Radiation pattern convergence is more easily observed when far-field and 3D FDTD solutions are superimposed on the same plot (Fig. 16). Large observation distances are necessary for convergence of radiation patterns near the critical angle. This is illustrated by plotting the position of H-plane radiation lobes as a function of relative dielectric permittivity and distance normalized by wavelength (Fig. 17) for relative permittivities ranging from 4 to 81. The peak amplitude pattern angle is plotted along the vertical axis and is defined as the angle made by the dominant peak in the H-plane as measured from the vertical axis. The angular position of H-plane radia-

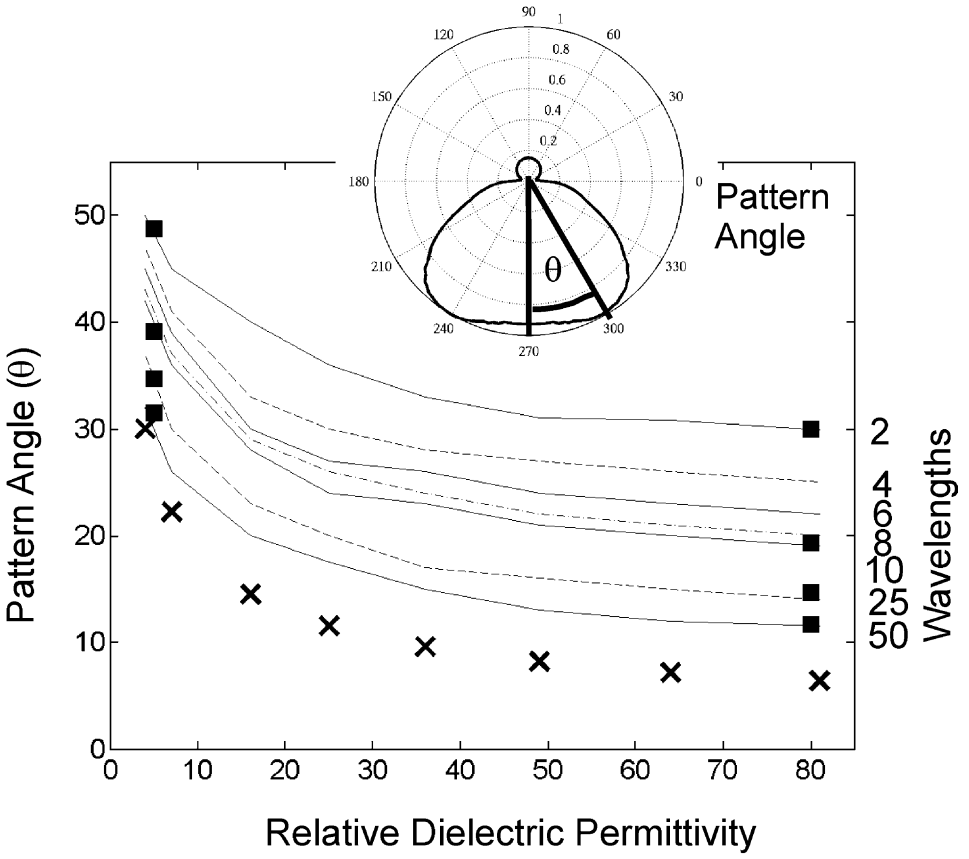

Fig. 17. FDTD computed H-plane radiation maxima as a function of relative dielectric permittivity ($\varepsilon_r = 4-81$) and distance normalized by wavelength. Asymptotic far-field solutions are denoted with the letter X. Independent results from van der Kruk (2002) for a relative permittivity of 5 and 80 at distances of 2, 10, 25, and 50 wavelengths are denoted with squares.

tion maxima decreases with increasing dielectric permittivity as predicted from critical angle calculations and far-field asymptotic patterns denoted with the letter X in Fig. 17. The rate of convergence of radiation maxima toward asymptotic far-field solutions decreases with observation distance (Fig. 17). The H-plane radiation patterns were computed using 3D FDTD simulations for wavelengths 2–10. Two-dimensional FDTD simulations were used for patterns computed at wavelengths 25 and 50 because of computational memory limitations. Because similar radiation maxima locations were observed for 2D and 3D simulations, we used 2D FDTD simulations to study the position of H-plane radiation maxima at observation distances beyond 10 wavelengths. Increased sidelobe intensity was observed in the 2D simulations and represents the most significant difference observed in H-plane patterns from the 2D and 3D simulations. Our results based on FDTD approximations of Maxwell's equations are validated by independent 3D modeling performed by van der Kruk (2002) using a numerical approximation of Sommerfeld's integral (van der Kruk, 2001) that is less memory intensive. The results from van der Kruk for a relative permittivity of 5 and 80 at distances of 2, 10, 25, and 50 wavelengths are denoted with squares. Like the 2D and 3D FDTD modeling, the two independent models (FDTD and numerical approximation) show similar angles for maximum radiation amplitudes.

5. Conclusions

GPR antenna patterns are a function of electrical properties and observation distance. Increasing dielectric permittivity and antenna height above the interface increases antenna pattern directivity in both near- and far-field simulations. The sharp peaks and notches characteristic of asymptotic far-field solutions are not observed in numerical simulations. While simulated H-plane radiation patterns maintain the approximately "triangular" shape of the far-field patterns, the near-field patterns are less angular and contain radiation maxima beyond the critical angle. The near-field radiation maxima move toward the far-field critical angle position with increasing distance. Both the near- and far-field E-plane radiation patterns contain a major lobe directly below the antenna. Two prominent sidelobes develop beyond the critical angle with increasing distance. E-plane amplitude lows located at the critical angle also become more pronounced with increasing distance from the antenna. Most of the discrepancy between far-field solutions and radiation patterns beyond a distance of 10 wavelengths occurs near the critical angle. While the "shape" of radiation patterns resembles far-field solutions beyond a distance of 10 wavelengths, H-plane radiation maxima and E-plane sidelobes occur at larger incidence angles than predicted by far-field solutions. Large observation distances are needed for complete convergence near the critical angle.

Physical measurements of radiation patterns using simple antennas show excellent agreement with FDTD simulations based on infinitesimal dipole models. GPR antennas commonly include features that influence radiation properties. Antennas are often shielded with a conductive cavity filled with absorber to reduce aboveground reflections and external noise. These modifications can affect antenna patterns and are specific to a particular antenna design. Unlike many other analytical and numerical solutions based on simple antenna geometries, FDTD simulations can readily be modified to model complex antenna geometries and targets. FDTD modeling also provides a valuable tool to understand and visualize wavefront propagation and scattering as a function of space and time. Improvements in computational resources and algorithms will make near-field solutions more widely available in the future. Accurate computation and understanding of radiation patterns will become more important as GPR advances and near-surface applications continue to proliferate.

Acknowledgements

We are grateful to Jan van der Kruk of the Swiss Federal Institute of Technology (formerly Delft University of Technology) for his radiation pattern simulations used to independently validate our results, for our many interesting and informative discussions, and manuscript review. FDTD modeling discussions with Kishore Rama Rao of the OSU ElectroScience Laboratory are gratefully acknowledged. A special thanks to Jens Munk for our many interesting and

informative electromagnetic discussions. We also thank Peter Annan of Sensors & Software and Steve Arcone of the US Army Cold Regions Research and Engineering Laboratory for their reviews that improved this manuscript.

References

Annan, A.P., 1973. Radio interferometry depth sounding: Part 1. Theoretical discussion. Geophysics 38 (3), 557–580.

Annan, A.P., Davis, J.L., 1976. Impulse radar sounding in permafrost. Radio Science 11, 383–394.

Annan, A.P., Waller, W.M., Strangway, D.W., Rossiter, J.R., Redman, J.D., Watts, R.D., 1975. The electromagnetic response of a low-loss, 2-layer, dielectric earth for horizontal electric dipole excitation. Geophysics 40 (2), 285–298.

Arcone, S.A., 1995. Numerical studies of the radiation patterns of resistively loaded dipoles. Journal of Applied Geophysics 33, 39–52.

Arcone, S.A., 1996. High resolution of glacial ice stratigraphy: a ground-penetrating radar study of Pegasus Runway, McMurdo Station, Antarctica. Geophysics 61 (6), 1653–1663.

Arcone, S.A., Delaney, A.J., 2000. GPR images of hidden crevasses in Antarctica. Proceedings of the Eighth International Conference on Ground Penetrating Radar, May 23–26, Gold Coast, Australia, SPIE, The International Society for Optical Engineering, Bellingham, WA, pp. 760–765.

Baker, G.S., 1998. Applying AVO analysis to GPR data. Geophysical Research Letters 25 (3), 300–397.

Bannister, P.R., 1982. The image theory of electromagnetic fields of a horizontal dipole in the presence of a conducting half-space. Radio Science 17, 618–626.

Baños, A., 1966. Dipole Radiation in the Presence of a Conducting Half-Space Pergamon, New York, NY.

Baumann, C.E., Sampaio, E.S., 2000. Electric field of a horizontal antenna above a homogeneous half-space: implications for GPR. Geophysics 65 (3), 823–835.

Davis, J.L., Annan, A.P., 1989. Ground-penetrating radar for high-resolution mapping of soil and rock stratigraphy. Geophysical Prospecting 37, 531–551.

Engheta, N., Papas, C.H., Elachi, C., 1982. Radiation patterns of interfacial dipole antennas. Radio Science 17 (6), 1557–1566.

Hoekstra, P., Delaney, A., 1974. Dielectric properties of soils at UHF and microwave frequencies. Journal of Geophysical Research 79 (11), 1699–1708.

Jiao, Y., McMechan, G.A., Pettinelli, E., 2000. In situ 2-D and 3-D measurements of radiation patterns of half-wave dipole GPR antennas. Journal of Applied Geophysics 43, 69–89.

King, R.W.P., Wu, T.T., Shen, L.C., 1974. The horizontal wire antenna over a conducting or dielectric half-space: current and admittance. Radio Science 9, 701–709.

Kunz, K.S., Luebbers, R.J., 1993. The Finite-Difference Time-Domain Method for Electromagnetics. CRC Press, Boca Raton, FL, 448 pp.

Lampe, B., Holliger, K., 2000. Finite-difference modeling of ground-penetrating radar antenna radiation. Proceedings of the Eighth International Conference on Ground Penetrating Radar, May 23–26, Gold Coast, Australia, SPIE, The International Society for Optical Engineering, Bellingham, WA, pp. 556–560.

Lampe, B., Holliger, K., 2001. Numerical modeling of a complete ground-penetrating radar system. Proceedings of SPIE, Subsurface and Surface Sensing Technologies and Applications III, vol. 4491. SPIE, The International Society for Optical Engineering, Bellingham, WA, pp. 99–110.

Lehmann, F., Boerner, D.E., Holliger, K., Green, A.G., 2000. Multicomponent georadar data: some important implications for data acquisition and processing. Geophysics 65 (5), 1542–1552.

Luebbers, R.J., Beggs, J., 1992. FDTD calculation of wide-band antenna gain and efficiency. IEEE Transactions on Antennas and Propagation 40 (11), 1403–1407.

Maloney, J.G., Smith, G.S., 1992. The efficient modeling of thin material sheets in the finite-difference time-domain (FDTD) method. IEEE Transactions on Antennas and Propagation 40 (3), 323–330.

Moran, M.L., Arcone, S.A., Greenfield, R.J., 2000. GPR radiation pattern effects on 3-D Kirchhoff array imaging. Proceedings of the Eighth International Conference on Ground Penetrating Radar, May 23–26, Gold Coast, Australia, SPIE, The International Society for Optical Engineering, Bellingham, WA, pp. 208–212.

Nehrbass, J.W., 1996. Advances in finite difference methods for electromagnetic modeling. PhD Dissertation, The Ohio State University, USA.

Norton, K.A., 1936. The propagation of radio waves over the surface of the earth and in the upper atmosphere: Part 1. Ground wave propagation from short antennas. Proceedings of the Institute of Radio Engineers 24 (10), 1367–1387.

Norton, K.A., 1937a. The physical reality of space and surface waves in the radiation field of radio antennas. Proceedings of the Institute of Radio Engineers 25 (9), 1192–1202.

Norton, K.A., 1937b. The propagation of radio waves over the surface of the earth and in the upper atmosphere: Part 2. The propagation from vertical, horizontal, and loop antennas over a plane earth of finite conductivity. Proceedings of the Institute of Radio Engineers 25 (9), 1203–1236.

Olhoeft, G.R., 1987. Electrical properties from 10^{-3} to 10^{+9} Hz—Physics and chemistry. Proceedings of the 2nd International Symposium on the Physics and Chemistry of Porous Media. American Institute of Physics Conference Proceedings, vol. 154, pp. 281–298.

Olhoeft, G.R., 1998. Electrical, magnetic, and geometric properties that determine ground penetrating radar performance. Proceedings of the Seventh International Conference on Ground Penetrating Radar, May 27–30. University of Kansas, Lawrence, KS, USA, pp. 177–182.

Radzevicius, S.J., 2001. Dipole antenna properties and their effects on ground penetrating radar data. PhD Dissertation, The Ohio State University, USA.

Reppert, P.M., Morgan, D.F., Toksöz, N.M., 2000. Dielectric constant determination using ground-penetrating radar reflection coefficients. Journal of Applied Geophysics 43, 189–197.

Roberts, R.L., 1994. Analysis and theoretical modeling of GPR polarization data. PhD Dissertation, The Ohio State University, USA.

Roberts, R.L., Daniels, J.J., 1996. Analysis of GPR polarization phenomena. Journal of Environmental & Engineering Geophysics 1 (2), 139–157.

Smith, G.S., 1984. Directive properties of antennas for transmission into a material half-space. IEEE Transactions on Antennas and Propagation AP-32 (3), 232–246.

Sommerfeld, A., 1909. Über die Ausbreitung der Wellen in der drahtlosen Telegraphie. Annalen der Physik 28, 665–737.

Turner, G., 1994. Modeling antenna–ground interactions. Proceedings of the Fifth International Conference on Ground Penetrating Radar, June 12–16, Kitchener, Ontario, Canada, vol. 1, Waterloo Center for Groundwater Research, University of Waterloo, Ont., pp. 205–221.

Valle, S., Zanzi, L., Sgheiz, M., Lenzi, G., Friborg, J., 2001. Ground penetrating radar antennas: theoretical and experimental directivity functions. IEEE Transactions on Geoscience and Remote Sensing 39 (4), 749–758.

van der Kruk, J., 2001. Three-dimensional imaging of multi-component ground penetrating radar data (http://www.tg.mp.tudelft.nl/~jvdkruk). PhD Dissertation, Delft University of Technology, Netherlands.

van der Kruk, J., 2002. Personal communication.

van der Kruk, J., Slob, E.C., 2000. The influence of the soil on reflections from above surface objects in GPR data. Proceedings of the Eighth International Conference on Ground Penetrating Radar, May 23–26, Gold Coast, Australia, SPIE, The International Society for Optical Engineering, Bellingham, WA, pp. 453–458.

van Gestel, J., Stoffa, P.L., 2000. Migration using multi-configuration GPR data. Proceedings of the Eighth International Conference on Ground Penetrating Radar, May 23–26, Gold Coast, Australia, SPIE, The International Society for Optical Engineering, Bellingham, WA, pp. 448–452.

Wait, J.R., 1962. Electromagnetic Waves in Stratified Media. Pergamon, New York, NY.

Wensink, W.A., Greeuw, G., Hofman, J., van Deen, J.K., 1990. Measured underwater near-field E-patterns of a pulsed, horizontal dipole antenna in air: comparison with the theory of the continuous wave, infinitesimal electric dipole. Geophysical Prospecting 38, 805–830.

Yee, K.S., 1966. Numerical solution of initial boundary value problems involving Maxwell's equations in isotropic media. IEEE Transactions on Antennas and Propagation AP-14 (3), 302–307.